HAL
open science

# An advanced electric propulsion diagnostic (AEPD) platform for in-situ characterization of electric propulsion thrusters and ion beam sources

Carsten Bundesmann, Christoph Eichhorn, Frank Scholze, Daniel Spemann, Horst Neumann, Damiano Pagano, Simone Scaranzin, Fabrizio Scortecci, Hans J Leiter, Sven Gauter, et al.

## To cite this version:

Carsten Bundesmann, Christoph Eichhorn, Frank Scholze, Daniel Spemann, Horst Neumann, et al.. An advanced electric propulsion diagnostic (AEPD) platform for in-situ characterization of electric propulsion thrusters and ion beam sources. The European Physical Journal D : Atomic, molecular, optical and plasma physics, 2016, 70 (10), pp.212. 10.1140/epjd/e2016-70236-0 . hal-03546638

**HAL Id: hal-03546638**

**https://hal.science/hal-03546638v1**

Submitted on 9 Feb 2022

**HAL** is a multi-disciplinary open access archive for the deposit and dissemination of scientific research documents, whether they are published or not. The documents may come from teaching and research institutions in France or abroad, or from public or private research centers.

L'archive ouverte pluridisciplinaire **HAL**, est destinée au dépôt et à la diffusion de documents scientifiques de niveau recherche, publiés ou non, émanant des établissements d'enseignement et de recherche français ou étrangers, des laboratoires publics ou privés.

**EPJ manuscript No.**
(will be inserted by the editor)

# An advanced electric propulsion diagnostic (AEPD) platform for characterization of electric propulsion thrusters and ion beam sources

Carsten Bundesmann[1], Christoph Eichhorn[1], Frank Scholze[1], Daniel Spemann[1], Horst Neumann[1], Damiano Pagano[2], Simone Scaranzin[2], Fabrizio Scortecci[2], Hans J. Leiter[3], Sven Gauter[4], Ruben Wiese[4], Holger Kersten[4], Kristof Holste[5], Peter Köhler[5], Stéphane Mazouffre[6], Richard Blott[7], Alexandra Bulit[8], and Käthe Dannenmeyer[8]

[1] Leibniz-Institute of Surface Modification, Permoserstr. 15, 04318 Leipzig, Germany
[2] Aerospazio Tecnologie s.r.l., Via Provinciale Nord 42a, 53040 Rapolano Terme, Siena, Italy
[3] Airbus Defence & Space GmbH, Im Langen Grund, 74239 Hardthausen-Lampoldshausen, Germany
[4] Christian-Albrechts-Universität zu Kiel, Leibnizstr. 11-19, 24098 Kiel, Germany
[5] Justus-Liebig-Universität Gießen, Heinrich-Buff-Ring 16, 35392 Gießen, Germany
[6] ICARE, CNRS, 1C Av. de la Recherche Scientifique, 45071 Orléans, France
[7] Space Enterprise Partnerships Ltd., Bennetts, Eastergate Lane, Chichester, West Sussex PO20 3SJ, United Kingdom
[8] ESA/ESTEC, Keplerlaan 1, 2201 AZ Noordwijk, The Netherlands

Received: date / Revised version: date

**Abstract.** Experimental characterization is an essential task in development, qualification and optimization process of electric propulsion thrusters or ion beam sources for material processing, because it can verify that the thruster or ion beam source fulfills the requested mission or application requirements, and it can provide parameters for thruster and plasma modeling. Moreover, there is a need for standardizing electric propulsion thruster diagnostics in order to make characterization results of different thrusters reliable and comparable. Therefore, we have developed an advanced electric propulsion diagnostic (AEPD) platform, which allows a comprehensive in-situ characterization of electric propulsion thrusters (or ion beam sources) and could serve as a standard on-ground tool in the future. The diagnostic platform uses a five-axis positioning system and provides the option to use diagnostic tools for beam characterization (Faraday probe, retarding potential analyzer, ExB probe, active thermal probe), for optical inspection (telemicroscope, triangular laser head), and for thermal characterization (pyrometer, thermocamera). Here we describe the capabilities of the diagnostic platform and provide first experimental results of the characterization of a gridded ion thruster RIT-$\mu$X.

**PACS.** XX.XX.XX No PACS code given

## 1 Introduction

Experimental characterization of electric propulsion (EP) thrusters or ion beam sources for material processing may provide important data both to judge their performance and to achieve a better understanding of physical processes in the plume and in the discharge chamber of such systems. Measurements of plasma parameters and monitoring of possible lifetime limiting alteration of the properties of thruster components, such as, for example, the evolution of the grid hole diameter in gridded ion thrusters, yield valuable information for the development and validation of numerical tools. Those codes, e.g. aiming at plasma and ion beam modeling (Examples: particle-in-cell code XOOPIC for charged particle and plasma simulation [1], IGUN code for simulation of the extraction of ions from a plasma [2]) or thruster lifetime prediction related to the erosion of ion thruster accelerator grids (Example: DynaSim code [3]), may finally help to partially circumvent expensive measurement campaigns with respect to thruster design and performance verification.

In this context, several groups have investigated surfaces of thruster components e.g. by telemicroscopy or thermal imaging methods [4–11]. In order to allow for the in-situ measurement of an extensive set of EP thruster performance parameters, the advanced electric propulsion diagnostic (AEPD) platform was designed and built some years ago [12,13]. The setup was modular and mobile such that it could be easily adapted to vacuum facilities of different size and experimental needs. Several measurement devices for particle beam and mechanical part characterization were implemented: a telemicroscope to measure erosion of mechanical parts, a triangular laser head to

*Send offprint requests to*: Corresponding author: C. Bundesmann; Electronic mail: carsten.bundesmann@iom-leipzig.de

monitor the geometric surface profile of selected parts of interest, a pyrometer to measure surface temperature distributions, an energy-selective mass spectrometer to collect energy distribution data and a Faraday probe for thruster plume characterization. A few sensors consisted of commercially available devices with in-house modifications, or were manufactured completely in-house (e.g. Faraday probe). The platform was tested successfully with two electric propulsion thrusters: a gridded ion thruster RIT-22 (Airbus Defence & Space, Germany, [7,10,12]) and a Hall effect thruster SPT-100D EM1 (EDB Fakel, Russia, [8,12]), in two different vacuum facilities.

The previous results demonstrated the capabilities of the first AEPD platform but also some limitations, mainly related to the design but also to financial needs. Therefore, a new activity has been started in order to improve the performance and availability of the AEPD platform. At present, the activities concentrate on three major topics: (i) The setup and test of additional or alternative plasma-diagnostic tools as extension or redesign of AEPD capabilities, (ii) the implementation of partially new designs of existing sensors in order to reduce the dimension and, hence, the interaction of diagnostic head and thruster, (iii) qualification of the AEPD platform as standard on-ground tool for EP thruster characterization. The first aspect deals with the development and integration of new sensors in the platform, such as a retarding potential analyzer, an ExB probe or an active thermal probe [13]. The second aspect concerns rather technical issues, such as modifications related to the vacuum compatibility of some diagnostic heads, size reduction and optimization of the respective sensor housings and working distance geometries as well as the protection of the sensor heads from damage due to ion bombardment [14].

In this paper, the most recent implementation of the diagnostic tools is described and first performance characterization results are presented, exemplary, for a gridded ion thruster RIT-$\mu$X (Airbus Defence & Space, [15]).

## 2 Experimental setup

### 2.1 Positioning system

The AEPD platform (see Fig. 1) consists of a 5-axis positioning system and several diagnostic tools. The positioning system utilizes a modular heavy bar setup, on which three UHV-specified linear tables with a traveling range of 700 mm and a traveling speed of typically 30 mm/s, and two UHV-specified rotary tables are mounted. The system can be easily adapted to chambers of different size. Using the linear and rotary tables, the thruster and the diagnostic heads can be positioned very precisely relative to each other, and even 1- and 2-dimensional mappings or angular-dependent measurements can be performed.

At present, the AEPD platform can be equipped with diagnostic tools for beam characterization (Faraday probe, retarding potential analyzer, ExB probe, active thermal probe), optical inspection (telemicroscope, triangular laser

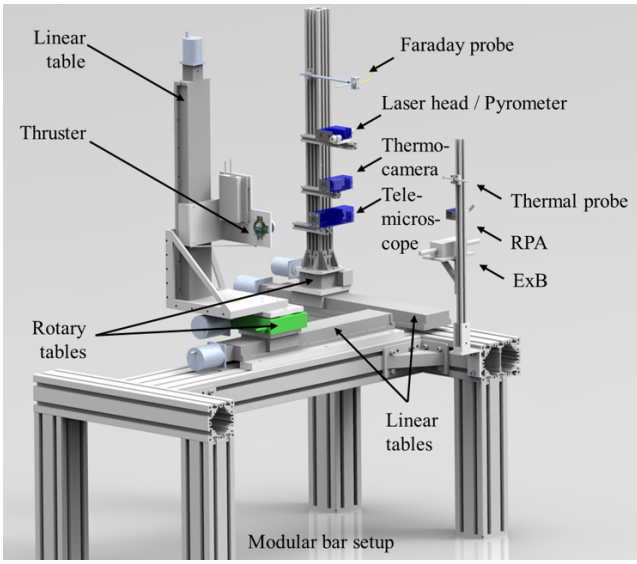


**Fig. 1.** Drawing of the AEPD platform with modular bar frame, linear and rotary tables, thruster and a possible configuration of diagnostic tools.

head) and thermal characterization (pyrometer, thermocamera). Table 1 lists the available diagnostic tools with measurement principle and possible applications. The main performance parameters of the diagnostic tools are summarized in Table 2. In the following, the diagnostic tools including their design are described in more detail.

### 2.2 Faraday probe

The Faraday probe has been developed in-house [16]. It uses a graphite ion collector rod, which is embedded in a ceramic tube surrounded by a thin metal cylinder of stainless steel with a length of 101 mm and an outer diameter of 6 mm. The ion collecting diameter is as small as 1.9 mm (area 2.8 mm$^2$) to allow for measurements with high spatial resolution. The ion collector is connected via a shielded BNC cable and a customized vacuum feedthrough to an external board with several high-precision resistors with different resistances. Thus, a large range of signal amplitudes can be covered. Data are recorded using a 12-bit analogue digital converter. With a sampling rate of up to 20 kHz, maximum ion current densities up to 40 mA/cm$^2$ with a resolution of 0.05 mA/cm$^2$ can be detected.

### 2.3 Retarding potential analyzer

The retarding potential analyzer was also developed in-house with the goal to make it as small as possible while keeping the performance (signal-to-noise ratio) sufficiently high. Therefore, a grid design with 149 holes has been chosen. It uses two grids for focusing the ion trajectories and for repelling secondary electrons, and an ion collector with cup shaped cavities, one for each ion channel. The first grid with hole diameters of 0.4 mm can also be used

**Table 1.** List of diagnostic tools with operation principle and possible measurement applications.

| Diagnostic tool | Specifications |
|---|---|
| Faraday probe | - Current density measurements<br>- Beam profiling |
| Retarding potential analyzer | - Electrostatic energy analyzer<br>- Energy distribution measurements of charged particles |
| ExB probe | - Ion velocity filter<br>- Velocity distribution measurements of charged particles<br>- Ion species fractions composition |
| Active thermal probe | - Energy flux density measurements<br>- Measurement of energy flux density distribution<br>- Detection of divergence and irregularities in the beam profile |
| Telemicroscope | - High-resolution optical imaging<br>- Inspection and radial erosion measurements of mechanical parts |
| Triangular laser head | - Distance measurements using the triangulation principal<br>- Surface profiling and axial erosion measurements of mechanical parts |
| Pyrometer | - Spot measurement of emitted infrared radiation<br>- Surface temperature measurements of mechanical parts |
| Thermocamera | - Imaged measurement of emitted infrared radiation<br>- Surface temperature images of mechanical parts |

for measuring the ion current density. The measurement area is 24 x 24 mm$^2$. The voltage for repelling the ions is applied to the ion collector. It can be varied between 0 V and 3000 V. The accuracy is better than 0.05 %. The collected ion current is transformed by a high-precision resistor into a voltage drop, which is measured by a 14-bit AD converter.

### 2.4 ExB probe

The ExB probe exploits the action of a magnetic (B) and an electric field (E) to select ions on the basis of their velocity $v_i$: only ions whose velocity satisfies the Wien condition (Eq. 1) are able to pass through the filter and thus being detected,

$$v_i = \frac{E}{B} = \frac{V_{\text{probe}}}{B \cdot d} \tag{1}$$

Because the velocity is a function of charge state $z_i$, mass $m_i$ and ion energy $E_{\text{ion,i}}$, different ion species can be separated. Eq. 2 expresses the electrodes voltage difference associated with each peak in the spectrum: On one hand a constant magnetic field is used to deflect ions trajectories, on the other hand a variable electric field acts for compensating the magnetic force, which allows ions with different velocity to be detected as a function of the voltage applied to electrodes. While in retarding potential analyzer measurements the voltage ramp to be applied to the retarding grid is directly connected to the accelerating voltage of the thruster, in case of the ExB probe the voltage range to be scanned depends also on the constructive parameters of the probe (magnetic field intensity, electrodes separation). These constructive parameters affect the performances of the probe in terms of resolution.

$$V_{\text{probe}} = B \cdot d \cdot \sqrt{\frac{2 z_i E_{\text{ion},i}}{m_i}} \tag{2}$$

The main aim was to develop a probe; which is able to put together high performances with low invasiveness. These aspects can be considered conflicting because an increase of the probe resolution can be determined by an increase of the magnetic field, and an increase of the magnetic field is usually associated with larger magnets. This problem was overcome by exploiting a particular magnetic configuration known as Stelter dipole allowing a significant increase of the magnetic field with respect to a traditional dipole with the same overall dimension. In particular, a maximum field of 0.54 T has been obtained for a probe having a 50 x 50 mm$^2$ section.

Another important aspect taken into account in the probe design concerns the topology of the magnetic and electric fields at the entrance and the exit of the probe. The different decaying behavior of the fields makes the probe not ideal, thus the Wien condition is no more satisfied in these regions. To overcome this problem the electrodes shape has been optimized in order to make the electric fringing field matching the magnetic one. The spatial resolution of the probe is determined by two collimators at the entrance and exit of the probe selecting ions traveling along a well-defined direction. A modular design approach has been implemented allowing to easily change the collimator length and the orifice diameter.

The probe is mainly used to determine the plasma composition in terms of ion species fraction because of the dependence of the ion velocity on the charge state. Assuming that all ion species are subject to the same accelerating voltage, the separation between the peaks position will be given by $\sqrt{z_i}$. The area under each peak yields

**Table 2.** Summary of selected specifications and performance parameters of the diagnostic tools.

| Diagnostic tool | Parameters |
|---|---|
| Faraday probe | - Sensor area diameter: 1.9 mm |
| | - Measurement range: up to 50 mA/cm$^2$ |
| | - Accuracy: $<$ 0.01 mA/cm$^2$ (depends on dynamic range) |
| | - Dimension: 82 mm (length), 5 mm (diameter) |
| Retarding potential analyser | - Number / diameter of holes: 149 / 1.8 mm |
| | - Measurement range: 0 eV $-$ 2000 eV |
| | - Accuracy: $<$ 5 eV |
| | - Dimension (including cover): 40 x 47 x 84 mm$^3$ |
| ExB probe | - Entrance orifice diameter: 1.6 mm |
| | - Entrance collimator length: 90 mm |
| | - Wien filter length: 150 mm |
| | - Resolution: 1000 m/s |
| | - Velocity range: up to 100000 m/s |
| | - Dimension: 50 x 50 x 280 mm$^3$ |
| Active thermal probe | - Measurement range: 1x10$^{-3}$ W/cm$^2$ $-$ 4 W/cm$^2$ |
| | - Sensitivity: $\pm$ 1x10$^{-3}$ W/cm$^2$ |
| | - Sensor dimension: 7 x 10 x 0.3 mm$^3$ |
| Telemicroscope | - Focal length / extension tube length*: 50 mm / 40 mm |
| | - Image size/working distance: 8.75 x 6.56 mm$^2$ / 112.5 mm |
| | - Resolution*: 1600 x 1200 pixel |
| | - Radial accuracy: $<$ 0.01 mm |
| | - Depth of field: $\pm$ 0.2 mm |
| | - Dimension (including cover): 60 x 70 x 210 mm$^3$ |
| Triangular laser head | - Spot size*: $<$ 0.2 mm (at a working distance of 150 mm) |
| | - Distance range*: 110 mm $-$ 190 mm |
| | - Repeatability*: $<$ 0.001 mm |
| | - Distance resolution: $<$ 0.01 mm |
| | - Dimension (including cover): 95 x 47 x 127 mm$^3$ |
| Pyrometer | - Spectral range*: 2.3 $\mu$m |
| | - Spot size*: 1.5 mm (at the focal distance of 110 mm) |
| | - Temperature range/resolution*: 150°C $-$ 1000°C / 0.1°C |
| | - System accuracy*: 0.3% of reading + 2°C |
| | - Repeatability*: 0.1% of reading + 1°C |
| | - Dimension (including cover): 25 x 30 x 47 mm$^3$ |
| Thermocamera | - Spectral range*: 7.5 $\mu$m $-$ 13 $\mu$m |
| | - Image size*: $\sim$ 0.05 m x 0.07 m (at a distance of 500 mm) |
| | - Resolution*: 160 x 120 pixel |
| | - Lateral resolution*: 1.5 mm (at a distance of 500 mm) |
| | - Temperature range/resolution*: 0°C $-$ 900°C / 0.1°C |
| | - System accuracy*: 2% of reading or 2°C |
| | - Dimension (including cover): 56 x 60 x 143 mm$^3$ |

* Numbers specified by the manufacturer.

the current carried by each ion species. Therefore, the ratio between this area and the area under the overall spectrum provides the current fraction (neglecting secondary emission effects). On the other hand the position of each peak is connected with the ion velocity through the constructive parameters of the probe: in particular the ion velocity distribution function for each ion species could be determined. This application requires a calibration of the probe providing a correction factor to be applied to the measured ion velocity to obtain the real one.

## 2.5 Active thermal probe

The active thermal probe (see Fig. 2) was developed during a previous project as a flexible diagnostic for the measurement of energy flux. For the use as a diagnostic tool for beam characterization as a part of the AEPD platform, it has been further improved and characterized especially regarding its sensitivity towards parasite heat sources.

The physical principle of the measurement method of the active thermal probe is based on the compensation of the incoming energy by decreasing the heating power of a preheated probe. The probe consists of a ceramic dummy-substrate (see Fig. 2(a)), which is electrically heated to a

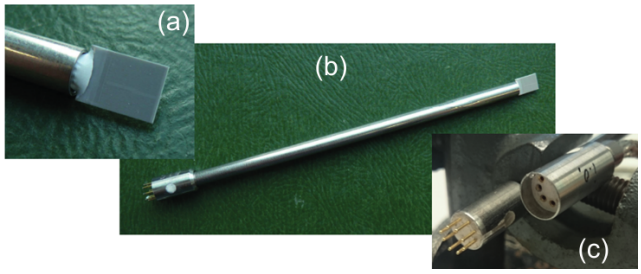


**Fig. 2.** Active thermal probe: Sensor area (a), full image (b) and connector (c) .

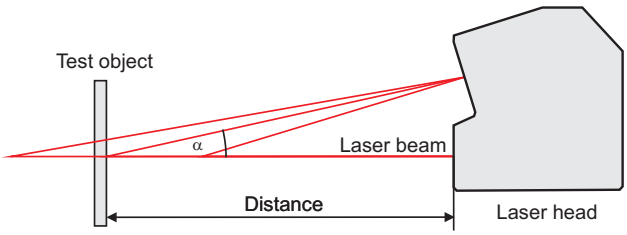


**Fig. 3.** Measurement principle of the triangular laser head (triangulation effect).

given set-point temperature. If the probe is exposed to an external energy flux (e.g. by the ion beam) the additional heating of the probe is compensated by a reduction of the electrical heating power, resulting in a constant temperature of the probe. The power of the external energy source is then directly given by the difference in the electrical heating power. In contrast to the other probes, the ATP measures both the contribution of charged and neutral particles. A much more detailed description of the working principle of the active thermal probe can be found in [17–19].

### 2.6 Telemicroscope and triangular laser head

The telemicroscope is a high-resolution optical camera, which can be used to measure radial (and axial) erosion of mechanical parts. It consists of a CCD camera, an extension tube and a photographic lens. By placing the extension tube between camera and lens, the radial resolution and depth of field is reduced considerably.

The triangular laser head measures the distance to a test object utilizing the triangulation effect, i.e. the fact that the detection angle $\alpha$ depends on the distance between triangular laser head and test object (see Fig. 3). When scanning across the test object, the surface profile can be measured, which gives access to axial (and radial) erosion.

Telemicroscope (The Imaging Source DFK 51AU02) and triangular laser head (Keyence LK-G152) are commercial devices. The triangular laser head is the same one that was used with the previous setup [12]. The telemicroscope has changed slightly with the goal to reduce the overall dimension. Now a smaller lens and a camera with a higher resolution is used. Triangular laser head and telemicroscope are operated inside vacuum. For safety reasons the devices are covered by a small housing each. The overall dimensions could be reduced considerably compared to the previous setup with vacuum-sealed housings[12]. The new housings consist of a metal base plate, a front plate made of graphite with sapphire window(s) and a metal cover. The window protects the optics from direct particle impingement. Additionally, the telemicroscope housing is equipped with four high-power LEDs for illumination. Figure 4 shows, exemplary, the housing of the telemicroscope.

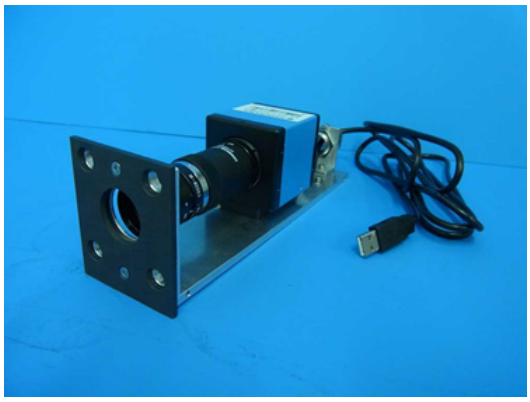

**Fig. 4.** Telemicroscope with housing (without metal cover).

**Fig. 5.** Pyrometer sensor head with housing.

### 2.7 Pyrometer and thermocamera

Pyrometer and thermocamera measure the surface temperature of a test object upon detection of the emitted infrared radiation. The physical principles are described by Planck's law, i.e. the intensity of the emitted infrared radiation is proportional to the surface temperature. When measuring the temperature, the properties of the test object, i.e. the emissivity of the material of interest, and of the setup, i.e. window effects, must be considered.

Pyrometer (Optris CT 3M) and thermocamera (Optris PI) are commercial devices. The pyrometer is different to the one, which was used in the previous setup [10,12], the thermocamera is new. Both devices were chosen because of

**Table 3.** Summary of operation parameters of the RIT-$\mu$X.

| Parameter | Operation point 1 | Operation point 2 |
|---|---|---|
| Beam Voltage | 1050 V | 1700 V |
| Beam Current | 4 mA | 8 mA |
| Accelerator voltage | -200 V | -250 V |
| Nominal thrust | 210 $\mu$N | 540 $\mu$N |

their small size, which reduces possible interactions with the energetic particle beam. Pyrometer and thermocamera are operated inside vacuum. Therefore, some vacuum-sensitive electronic parts (capacitors) had to be replaced or removed (liquid crystal display). Both diagnostic heads are placed inside metal housings with appropriate windows (pyrometer: sapphire window; thermocamera: ZnS window) for safety reasons [14]. The housing of the pyrometer is shown in Fig. 5, the housing of the thermocamera is similar to that of the telemicroscope in Fig. 4.

Operating the diagnostic heads inside vacuum has the advantage that they can be brought closer to the test object. A smaller working distance results in a better lateral resolution, which is especially favorable for the thermocamera.

### 2.8 Thruster

A gridded ion thruster RIT-$\mu$X [15] was used for the test measurements. Radio-frequency ion thrusters (RITs) generate thrust in two steps: In the first step the propellant is ionized in the oscillating electromagnetic field of a coil (plasma). Once ionized, the propellant is accelerated in the electrostatic field of the thruster's second functional unit called the grid system.

The ionization chamber of the RIT-$\mu$X has an inner diameter of 4 cm at the interface to the grid system and a length of 3 cm. Its inductively coupled plasma is operated with a frequency of 2.5 MHz. The experiments were performed using the standard propellant Xenon. The RIT-$\mu$X can be equipped with different sets of grids optimized for specific mission requirements. During the reported tests a configuration with 37 extraction channels was used. It is designed for extraction voltages in the range from 600 V to 2200 V and nominal ion currents between 1 mA and 10 mA. The thruster was operated here at two operation points as summarized in Table 3.

### 2.9 Test chamber

The tests were performed in the Jumbo test facility [20]. The tank is of cylindrical shape with a diameter of 2.6 m, a length of 6 m and a volume of 30 m$^3$. It is equipped with turbo and cryo pumps with a total pumping speed of 120.000 l/s. The base pressure is about 1 x $10^{-7}$ mbar.

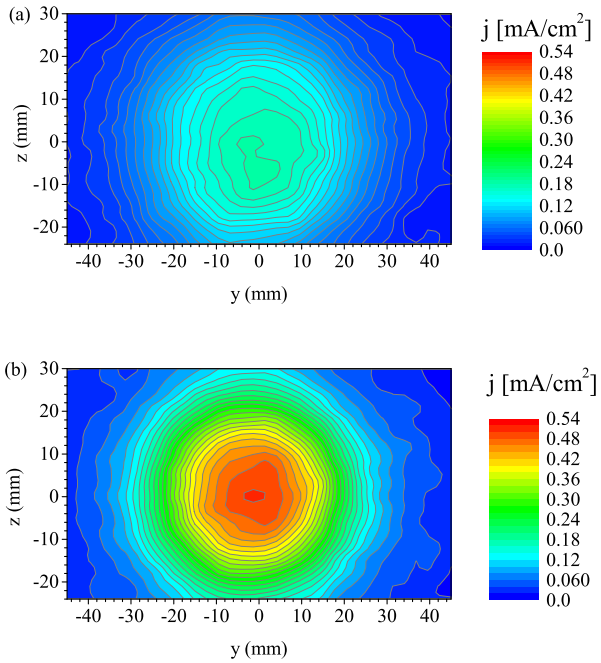


**Fig. 6.** Current density maps of the RIT-$\mu$X at operation point 1 (a) and operation point 2 (b) measured with the Faraday probe at a distance of 120 mm to the exit plane of the thruster.

## 3 Results

### 3.1 Faraday probe

Selected current density maps of the thruster at the two operation points are plotted in Fig. 6. As expected, rotationally symmetric, Gaussian shaped beam profiles can be seen with a higher maximum current density at operation point 2 ($j_{\max}$ = 0.52 mA/cm$^2$) than at operation point 1 ($j_{\max}$ = 0.18 mA/cm$^2$). This is related to the higher beam voltage at operation point 2. The full width at half maximum of the beam profiles is very similar for the two operation points (operation point 1: 48.0 mm; operation point 2: 40.8 mm).

### 3.2 Retarding potential analyzer

The energy distribution of the extracted ions was measured at the two operation points, too. Figure 7 shows, exemplary, the result for operation point 1. The energy distribution reveals only a single peak. The peak position is at the beam voltage and the width at half maximum is smaller than 20 V, which corresponds to less than 2 % of the ion energy. Ions with other energies, which could be generated by charge exchange processes, or multiply charged ions were not detected.

### 3.3 ExB probe

Ion velocity measurements were performed with the ExB probe positioned along the thruster axis at a distance

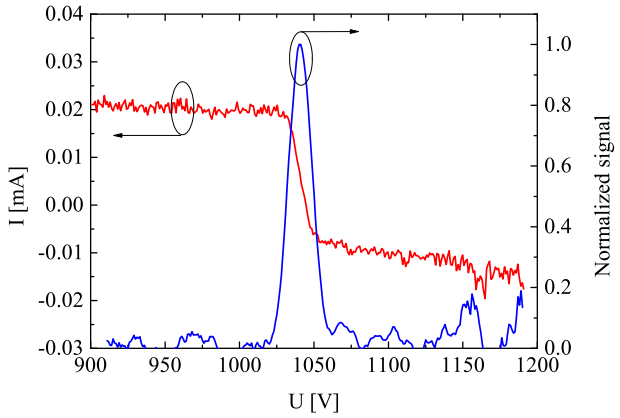


**Fig. 7.** Current signal (red curve) measured with the retarding potential analyzer and calculated energy distribution (blue curve) of the extracted ions, exemplary, for operation point 1.

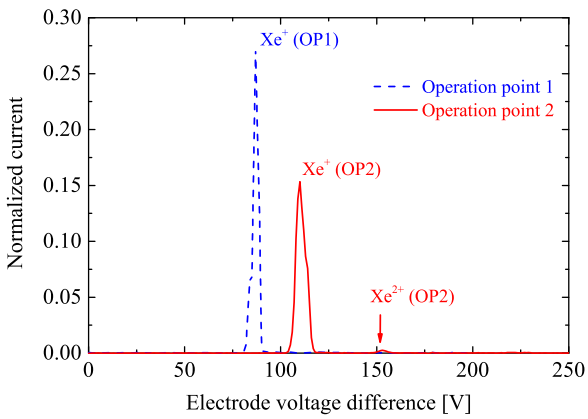


**Fig. 8.** ExB probe normalized spectra at operation point 1 (dashed blue line) and operation point 2 (solid red line) at a distance of 350 mm to the exit plane of the thruster.

of 350 mm from the thruster exit plane. Figure 8 shows two spectra obtained for the two operation points of the thruster. The position of the peaks corresponds to the different ion velocity, which is proportional to the square root of the ion energy. The most pronounced peaks at an electrode voltage difference of $\sim$ 87 eV (operation point 1) and $\sim$ 111 eV (operation point 2) can be assigned to singly charged ions ($Xe^+$). As expected, the ratio of the peak positions is (approximately) the same as the square root of the ratio of the corresponding beam voltages. In the curve for operation point 2 a second peak at an electrode difference voltage of $\sim$ 153 eV can be seen. This peak is related to doubly charged ions ($Xe^{2+}$). The peak is very small, i.e. the fraction of doubly charged ions is low, as it is typical for gridded ion thrusters.

### 3.4 Active thermal probe

In Fig. 9 selected results for the measurement of the energy flux density under variation of the vertical position

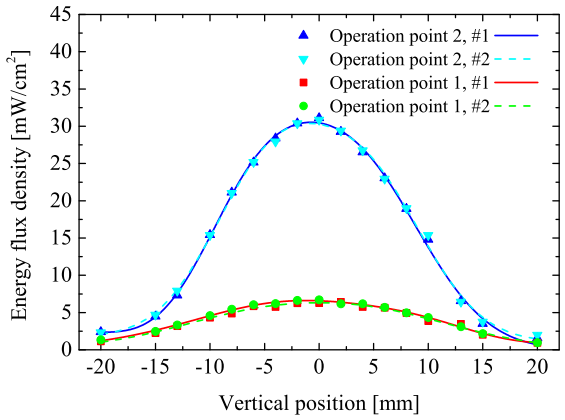


**Fig. 9.** Energy flux density vs. vertical position for the RIT-$\mu$X running at operation point 1 and 2 measured with the active thermal probe. The symbols represent the experimental data, the solid lines give cubic spline interpolations as a guide to the eye. The are two measurements for each operation point.

relative to the center axis of the thruster are presented. The thruster was aligned in such a way that the beam hits the probe at normal incidence and that the center of the thruster grid has a distance of 490 mm to the probe. Figure 9 summarizes the results of two measurements for the two thruster operation points each. The data illustrate clearly that the measurements show a good reproducibility and give access to the radial distribution of the energy flux density of the beam. Furthermore it should be pointed out that even close to its lower detection limit of 1 mW/cm$^2$ the probe gives reproducible results.

### 3.5 Telemicroscope

In Figs. 10 and 11 two telemicroscope images are shown. Figure 10 depicts an eyepiece graticule test structure, which is used for principal characterization and calibration purposes. It was found that the field of view is 8.75 x 6.56 mm$^2$ at a working distance of 112.5 mm. The depth of field is smaller than $\pm$0.5 mm and the lateral (radial) resolution is better than 0.01 mm. The second image in Fig. 11 shows a section of the grid of the thruster (thruster is off). The grid holes can be clearly resolved and grid hole diameter and, hence, the grid hole erosion are accessible. The diameter of the center hole in Fig. 11 is 1.27 mm $\pm$ 0.02 mm.

### 3.6 Triangular laser head

Figure 12 shows a surface profile scan of the thruster. Among others, the grid hole area can be identified clearly and the number of holes can be seen. Doing so, the principal shape of the grid including, for instance, its radius of curvature could be measured [7,10]. In case of the RIT-$\mu$X the grid is flat. However, there are experimental limitations due to the measurement principle (triangulation

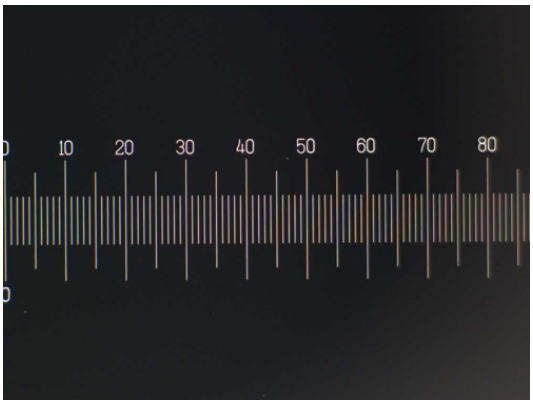


**Fig. 10.** Telemicroscope image of an eyepiece graticule test structure.

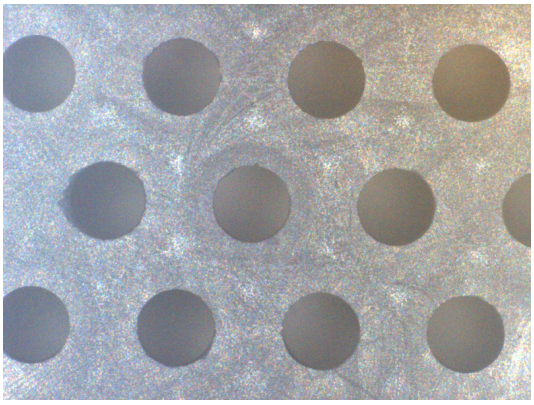

**Fig. 11.** Image of grid holes of the RIT-$\mu$X taken with the telemicroscope.

effect). Because of that, the triangular laser head might fail in measuring the profile at steep or abrupt edges (see detail inset in Fig. 12).

### 3.7 Thermocamera

Figure 13 (a) shows a thermocamera image of the RIT-$\mu$X operated at operation point 2. The surface temperature of almost the whole thruster is imaged. The temperature distribution is nearly homogeneous, apart from the holes. As shown in previous tests, the temperature of the plasma chamber, which is imaged through the holes is considerably higher than the grid surface temperature[7,10]. In Fig. 13 (b) two temperature line scans, which were extracted from thermocamera image, are plotted. The grid temperature was found to be 68°C ± 2°C.

## 4 Discussion

The experimental data demonstrate impressively the capabilities of the AEPD platform, which allows a comprehensive characterization of electric propulsion thrusters or ion beam sources for material processing.

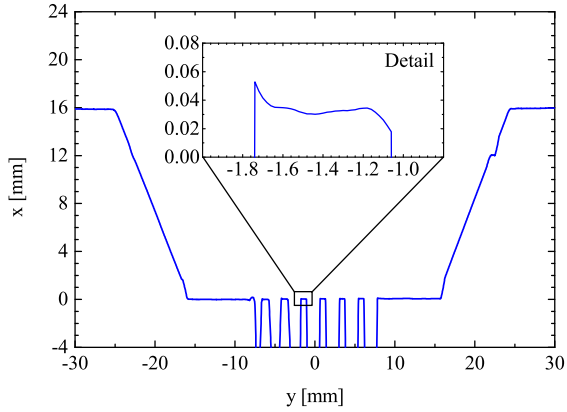


**Fig. 12.** Surface profile scan across the center of the RIT-$\mu$X measured with the triangular laser head. The detail inset shows the measured surface profile scan between two grid holes. The rise of the profile at the left side is a measurement artifact due the triangulation measurement principle.

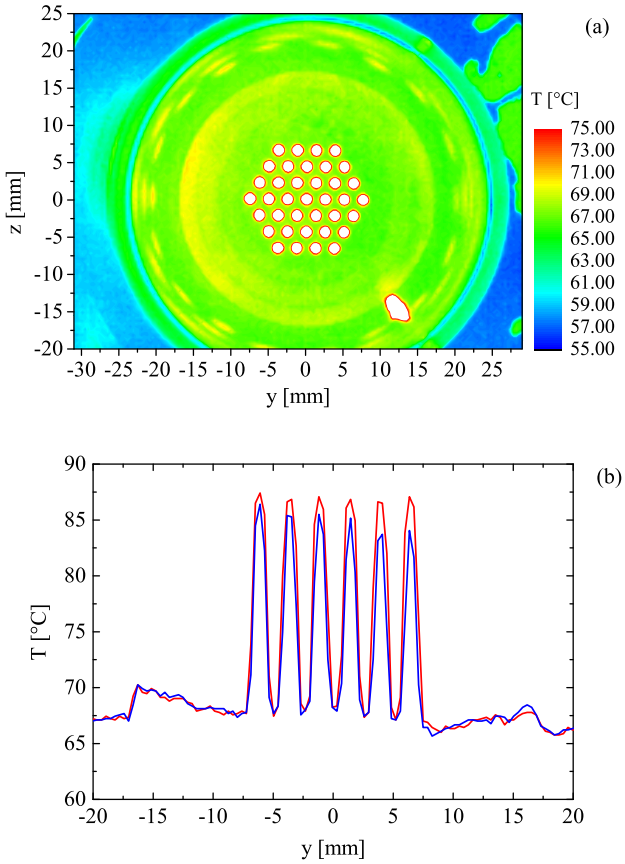


**Fig. 13.** (a) Thermocamera image of the RIT-$\mu$X at operation point 2. (b) Horizontal temperature scans across the center of the thruster extracted from thermocamera image in panel (a).

Typically, the main focus lies on investigating beam properties, because the beam provides the thrust or, in material science, the tool for material modification. Important parameters are particle energy or velocity, beam shape and divergence, composition, charge state. All of these parameters can be measured with the current setup. It is not only possible the measure the properties of charged particles (Faraday probe, retarding potential analyzer, ExB probe) but also of energetic neutrals (active thermal probe).

The optical inspection tools (triangular laser head, telemicroscope) provide important information about the shape of mechanical parts and its evolution in time (erosion), which can be life-limiting factors. The triangular laser head is advantageous when measuring axial dimensions, whereas the telemicroscope has its advantage when measuring radial dimensions. However, both devices can be used to measure axial and radial dimensions, though with different accuracy.

Thermal characterization is important, for instance, for evaluating the thermal impact on the performance of satellites (in case of electric propulsion thrusters). Both pyrometer and thermocamera provide similar information. In case of small thrusters, the thermocamera can yield a full thermal image. In case of larger thrusters (with higher power), scanning with the pyrometer seems to be more appropriate due to its smaller dimension.

## 5 Summary and Outlook

We have reported about improvements of our AEPD platform. The activities are focused on modifying the experimental setup in order to reduce possible interactions between diagnostics and thruster, on implementing additional or alternative diagnostic heads in order to improve the performance or to expand the portfolio of accessible parameters. We have described the main parameters of the new diagnostic tools and presented first experimental results, exemplary, with a gridded ion thruster RIT-$\mu$X. Future work will be focused on detailed analysis of all sources of uncertainty in order to make progress in direction of standardization of electric propulsion diagnostics. Standardization requires traceable standards. Unfortunately, the availability of traceable standards is limited, especially, when it comes to operation inside vacuum. However, if there is no standard then a procedure or tool must be definded, which can serve as a reference. Standardization is an essential part in promoting electric propulsion technologies

## Acknowledgements

The work was performed with financial support provided by ESA/ESTEC under contract No. 4000107451/12/NL/RA "Qualification of the AEPD System as a Standard On-Ground Tool for Electric Propulsion Thrusters". The authors thank R. Woyciechowski, M. Müller, S. Daum (all Leibniz-Institute of Surface Modification), R. Kukies (Airbus Defence & Space), W. Gärtner, U. Bachmann (all Justus-Liebig-Universität Gießen) for technical support.

## Author contribution statement

All authors contributed equally to the paper.

## References

1. J.P. Verboncoeur, A.B. Langdon, N.T. Gladd, Comp. Phys. Comm. **87**, (1995) 199.
2. R. Becker and W. B. Herrmannsfeldt, Rev. Sci. Instrum. **63**, (1992) 2756.
3. M. Tartz, E. Hartmann, H. Neumann, Rev. Sci. Instrum. **79**, (2008) 02B905.
4. M. Crofton, R. Ueunten, L. Harris, E. Yohnsee, R. Cohen, Proc. 32nd AIAA Joint Propulsion Conference and Exhibit, Lake Buena Vista, 1996, Paper AIAA-96-2977.
5. S. Mazouffre, F. Dubois, M. Dudeck, P. Echegut, Proc. 4th International Spacecraft Propulsion Conference, Cagliary, 2004. Paper 2004-ESA-SP.555E-26M.
6. S. Mazouffre, J. Perez-Luna, D. Gawron, M. Dudeck, P. Echegut, Proc. 29th International Electric Propulsion Conference, Princeton, 2005, Paper IEPC-2005-063.
7. C. Bundesmann, M. Tartz, F. Scholze, H. Neumann, H.J. Leiter, F. Scortecci, D. Feili, P.E. Frigot, J. Gonzalez del Amo; Proc. 31st International Electric Propulsion Conference, Ann Arbor, 2009, Paper IEPC-2009-160.
8. C. Bundesmann, M. Tartz, F. Scholze, H. Neumann, F. Scortecci, S. Scaranzin, P.E. Frigot, J. Gonzalez del Amo, R.Y. Gnizdor; Proc. 31st International Electric Propulsion Conference, Ann Arbor, 2009, Paper IEPC-2009-141.
9. T. Misuri, A. Milani, M. Andrenucci, Proc. 31st International Electric Propulsion Conference, Ann Arbor, 2009, Paper IEPC-2009-036.
10. C. Bundesmann, M. Tartz, F. Scholze, H. Neumann, H.J. Leiter, F. Scortecci; J. Propul. Power **27**, (2011) 532.
11. T. Misuri, T. Vrebosch, L. Pieri, M. Andrenucci, M. Tordi, E. Marcuzzi, M. Batolozzi, S. Renzetti, J. Gonzalez del Amo, Proc. 32nd International Electric Propulsion Conference, Wiesbaden, 2011, Paper IEPC-2011-129.
12. C. Bundesmann, M. Tartz, F. Scholze, H.J. Leiter, F. Scortecci, R.Y. Gnizdor, H. Neumann; Rev. Sci. Instrum. **81**, (2010) 046106.
13. D. Pagano, F. Scortecci, C. Bundesmann, C. Eichhorn, F. Scholze, H. Neumann, H. Leiter, H. Kersten, S. Gauter, R. Wiese, R. Blott, P.J. Klar, K. Holste, B. Meyer, S. Mazouffre, A. Bulit, J. Gonzales del Amo; Proc. 34th International Electric Propulsion Conference, Hyogo-Kobe, 2015, Paper IEPC-2015-363.
14. C. Bundesmann, C. Eichhorn, F. Scholze, H. Neumann, H.J. Leiter, F. Scortecci; Proc. 34th International Electric Propulsion Conference, Hyogo-Kobe, 2015, Paper IEPC-2015-392.
15. C. Altmann, H. Leiter, R. Kukies; Proc. 34th International Electric Propulsion Conference, Hyogo-Kobe, 2015, Paper IEPC-2015-274.
16. C. Eichhorn, F. Scholze, C. Bundesmann, H. Neumann; Proc. 33rd International Electric Propulsion Conference, Washington, 2013, Paper IEPC-2013-295.

17. R. Wiese, Dissertation, Ernst-Moritz-Arndt Universität, Greifswald, 2008.
18. R. Wiese, H. Kersten, G. Wiese, M. Häckel, Vakuum in Forschung und Praxis **23**(3), (2011) 20.
19. R. Wiese, H. Kersten, G. Wiese, R. Bartsch, EPJ Techniques and Instrumentation **2**, (2015) 2.
20. P.J. Klar, K. Hannemann, U. Ricklefs, H. Leiter Proc. 34th International Electric Propulsion Conference, Hyogo-Kobe, 2015, Paper IEPC-2015-89.